Table 1 33 screened patients with MYCN amplification

Case No.	MYCN	Stage	Surgery	Chemotherapy	Radio therapy	Mega therapy	Outcome	Follow-up (year)
1	150	3	CE	VCR, CPM	(−)		NED	0.8
2	>100	4	B	VCR, CPM, VP-16, ADR, CDDP, DTI C	(−)		Tumour death	0.3†
3	55	4	CE	CPM, VP-16, THP-ADR, CDDP, L-PAM, CBDCA	(−)	Auto-BMT	NED	5.3
4	50	4	CE	(+)	(+) 25 gy	PBSCT	Tumour death	2.3†
5	50	4	CE	(+)	(−)		Tumour death	0.7†
6	29	4	CE	CPM, VP-16, THP-ADR, CDDP	(−)	PBSCT	Therapy complication	1.0†
7	24	2	CE	VCR, CPM, VP-16, THP-ADR, CDDP	(−)		NED	5.9
8	20	2	CE	CPM, VP-16, THP-ADR, CDDP	(+) 20 gy	PBSCT	Tumour death	2.7†
9	15	4s	CE	(+)	(−)	Auto-BMT	NED	5.1
10	14	4	B	CPM VP-16, THP-ADR CDDP→refuse	(+) 12 gy		Tumour death	2.5†
11	12	4	CE	(+)	(−)	CBSCT	NED	2.0
12	10	3	CE	VCR, CPM, CDDP, VP-16	(+) 10 gy		NED	3.30
13	10	4s	CE	CPM, VP16, THP-ADR, CDDP	(−)		NED	4.7
14	6	4s	CE	CPM, VP16, THP-ADR, CDDP	(−)		NED	5.0
15	5.7	3	B	VCR, CPM, VP-16, THP-ADR, CDDP	(+) 30 gy		Tumour death	0.9†
16	5	2	CE	VCR, CPM	(+) 24 gy		NED	10.2
17	5	2	CE	VCR, CPM, ADR, CDDP	(−)		NED	8.1
18	4–5	4	CE	VCR, CPM, THP-ADR, CDDP	(−)		NED	8.8
19	4	1	CE	VCR, CPM	(−)		NED	6.6
20	4	1	CE	VCR, CPM	(−)		NED	8.7
21	4	1	CE	VCR, CPM	(−)		NED	6.1
22	4	3	PE	CPM, VP-16, ADR, CDDP	(−)		NED	7.5
23	3.7	4s	CE	VCR, CPM, ADR, CDDP	(−)		NED	6.8
24	3	1	CE	(−)	(−)		NED	5.7
25	3	1	CE	(−)	(−)		NED	5.0
26	3	2	CE	VCR, CPM, THP-ADR, CDDP	(−)		NED	4.5
27	3	2	CE	(−)	(−)		NED	6.0
28	3	3	B	CPM, VP-16, THP-ADR, CDDP	(−)		NED	5.1
29	3	3	CE	VCR, CPM, VP-16, THP-ADR, CDDP	(−)	Auto-BMT	NED	2.1
30	3	3	CE	(−)	(−)		Tumour death	0.9†
31	3	4	CE	CPM, THP-ADR, CDDP	(−)		NED	8.7
32	3	4s	CE	(+)	(−)		NED	7.8
33	2–4	4	B	VCR, CPM, THP-ADR, CDDP	(−)		NED	9.7

by the MSPN had biologically favourable factors, such as no-deletion of 1p and low expression of the *TRK-A* gene, some cases with unfavourable prognostic factors have been reported (Matsunaga *et al*, 2000; Tajiri *et al*, 2001). *MYCN* is one of the most important prognostic factors in NB (Rubie *et al*, 1997; Tonini *et al*, 1997). How *MYCN* is related to the prognosis and clinical features of infantile cases, especially those discovered by MSPN, is not clear. Our large-scale study clarified the frequency and clinical features, including the prognoses, of the infantile NB cases with MNA detected that were detected by MSPN.

Among 1533 cases discovered by the MSPN, 33 cases (2.2%) showed MNA. This frequency is much lower than the 15–22% frequency of MNA cases reported in the United States and Europe (Tonini *et al*, 1997; Brodeur, 2003). In addition, in infants that were less than 1-year-old, the frequency of MNA in our study was lower than that reported in Italy (6.8%) (Tonini *et al*, 1997). This suggests that the MSPN detected a greater number of tumours that spontaneously regressed and/or matured than did the clinical examinations.

MYCN is the powerful prognostic factor in infants whose NB was discovered by the MSPN. The 3-year EFS rates (46%) and 4-year OS rates (53%) for patients with MNA were significantly lower than those for patients without MNA (99.3 and 99%, respectively) ($P<0.001$). According to our previous investigation, the 4-year OS rate for cases less than 12 months old with MNA of over 10 copies, which include clinically detected cases, was 41% (Ikeda *et al*, 2002). The prognosis of cases with MNA detected by MSPN might be comparatively good though prognoses cannot be compared because the researches the survival rates of cases detected clinically and cases detected by MSPN did not investigated at the same time. The infants with MNA that were detected by MSPN might be considered to have benefited from the early detection provided by the screening. Indeed, among patients with MNA, the 3-year EFS rates (93.3%) of patients in stages I, II and IVs were significantly higher than those in stages III and IV (58.3%). If these cases with MNA were not discovered in the early stage by MSPN, some malignant components of tumours would proliferate and progress. As a result, the tumours would be discovered clinically after the patients were 1-year-old. However, the number of cases with MNA is only a very small proportion (2.2%) of the total cases discovered by MSPN. In addition, it is clear that the number of NB patients increased by introduction of MSPN. Therefore, the effectiveness of MSPN discovery of patients with MNA is unclear.

Furthermore, tumours detected by MSPN might regress spontaneously (Yamamoto *et al*, 1998). Several institutions in Japan recently adopted a conservative approach (the 'wait and see' approach), in which children discovered to have stage I, II or IVs tumours by the MSPN were not given any therapeutic treatment in the expectation that the tumour would spontaneously regress (Yamamoto *et al*, 1998). However, a careful follow-up is necessary in cases detected by MSPN, because some of the cases were found to have MNA in the early stage. Most cases with MNA in this study did not have higher urinary VMA levels than without MNA and then, they were not predicted to have a poor clinical outcome at their initial onset. Even in the early stages (stages I, II and IVs), biopsies are required in order to determine the biological prognostic factors of the tumour.

Moreover, in this study, it became clear that patients with MNA of three to nine copies also had poor prognoses. *MYCN* gene has

Table 2 Characteristics of patients with and without *MYCN* amplification detected by mass screening for neuroblastoma

Patient characteristics	Number of cases (%) MNA (>10) ($n=13$)	MNA (3–9) ($n=20$)	MNA (−) ($n=1500$)	*P*-value	MNA (+, >3) 3-yr EFS	*P*-value
Tumour stage						
I	0 (0)	5 (25)	595 (40)	$P<0.001^a$, $P=0.05^b$	100	$P=0.021$
II	2 (15)	5 (25)	463 (31)	(1,2,4s/3,4)	86	(1,2,4s/3,4)
III	2 (15)	5 (25)	280 (19)		71	
IV	7 (54)	2 (10)	65 (4)		44	
IVs	2 (15)	3 (15)	97 (6)		100	
Gender						
Female	3 (23)	11 (55)	722 (49)	$P=0.043^a$, $P=0.579^b$	86	
Male	11 (77)	9 (45)	764 (51)		68	
Primary site						
Adrenal gland	12 (92)	13 (65)	764 (51)	$P=0.002^a$, $P=0.131^b$	68	$P=0.021$
Other abdominal	0 (0)	3 (15)	456 (30)	(adrenal gland/other site)	100	(adrenal gland/other site)
Chest	1 (8)	3 (15)	224 (15)		100	
Pelvis	0 (0)	1 (5)	50 (3)		100	
Neck	0 (0)	0 (0)	6 (0)			
VMA						
$<20\ \mu g\,mgCr^{-1}$	3 (23)	4 (20)	293 (20)		100	
$21-100\ \mu g\,mgCr^{-1}$	7 (54)	15 (75)	982 (67)		82	
$>101\ \mu g\,mgCr^{-1}$	2 (15)	1 (5)	184 (13)		75	
	(mean:			74.6 $\mu g\,mgCr^{-1}$)	(mean: 54.8 $\mu g\,mgCr^{-1}$)	(mean: 54.4 $\mu g\,mgCr^{-1}$)
$P=0.985^a$, $P=0.977^b$		$P=0.364$				
HVA						
$<20\ \mu g\,mgCr^{-1}$	0 (0)	2 (10)	206 (14)		100	
$21-100\ \mu g\,mgCr^{-1}$	7 (54)	16 (80)	1084 (74)		78	
$>101\ ng\,mgCr^{-1}$	6 (46)	2 (10)	170 (12)		63	
	(mean:			107.1 $\mu g\,mgCr^{-1}$)	(mean: 66.0 $\mu g\,mgCr^{-1}$)	(mean: 55.6 $\mu g\,mgCr^{-1}$)
$P=0.008a$, $P=0.371^b$		$P=0.478$				
NSE						
$<15\ ng\,ml^{-1}$	5 (38)	9 (45)	526 (47)		93	
$16-100\ ng\,ml^{-1}$	2 (15)	7 (35)	568 (51)		89	
$>101\ ng\,ml^{-1}$	6 (46)	2 (10)	14 (1)		25	
	(mean: 266.9 $ng\,ml^{-1}$)	(mean: 32.6 $ng\,ml^{-1}$)	(mean: 26.2 $ng\,m^{-1}$l)	$P=0.049^a$, $P=0.285^b$		$P=0.0005$
Ferritin						
$<30\ ng\,ml^{-1}$	2 (15)	5 (25)	506 (54)		100	
$31-100\ ng\,ml^{-1}$	5 (38)	8 (40)	383 (41)		69	
$>101\ ng\,ml^{-1}$	6 (46)	1 (5)	54 (6)		43	
	(mean: 167.3 $ng\,ml^{-1}$)	(mean: 55.9 $ng\,ml^{-1}$)	(mean: 33.7 $ng\,ml^{-1}$)	$P=0.025^a$, $P=0.032^b$		$P=0.174$

[a]*P*-value between MNA (>10) and MNA (−). [b]*P*-value between MNA (3–9) and MNA (−).

been analysed by the Southern blotting method for whole tumours, but this method is not able to evaluate the status MNA in individual NB cells. While, the FISH method is able to evaluate MNA individual tumour cells, however, it is difficult to determine the copy number of MNA by the FISH method. *MYCN* amplification was defined as a more than the fourfold increase of *MYCN* signals in relation to the number of chromosomes 2 in FISH method. Moreover, additional copies up to the fourfold were defined as *MYCN* gain (Spitz *et al*, 2004). Spitz reported that 6% of tumours displayed *MYCN* gain and this *MYCN* gain was associated only with a poor outcome in localized or 4s NB cases (Spitz *et al*, 2004). In our study, these patients with MNA of three to nine copies might suggest the *MYCN* gain rather than *MYCN* amplification. In cases 4 and 30, MNA were confirmed by FISH method, however, in all the cases MNA were not confirmed by it. *MYCN* amplification must be determined by adding the FISH method in these cases (Mathew *et al*, 2001).

In the studies of the USA group (COG) and the German group, the therapeutic strategy of surgical resection or observation is recommended for NB patients in stages I or II, regardless of the presence of MNA (Cohn *et al*, 1995; Kawa *et al*, 1999; Berthold and Hero, 2000; Perez *et al*, 2000). However, in Japan, patients with MNA of more than 10 copies are classified as being in a high-risk group. In the protocol for high-risk NB, patients receive intensive chemotherapy combined with stem cell transplantation (Kawa *et al*, 1999; Kaneko *et al*, 2002). Infantile NB patients with MNA as well as patients in the high-risk group more than 1-year-old with MNA of over 10 copies have been receiving intensive chemotherapy (Matsumura and Michon, 2000). In our study 29 of 33 cases with MNA received chemotherapy regardless of the stage. The use of chemotherapy might improve the prognosis of patients with MNA. In the cases with MNA over 10 copies, the treatment strategy including more intensive chemotherapy might be necessary, because five cases except one died of progressive disease. For cases with

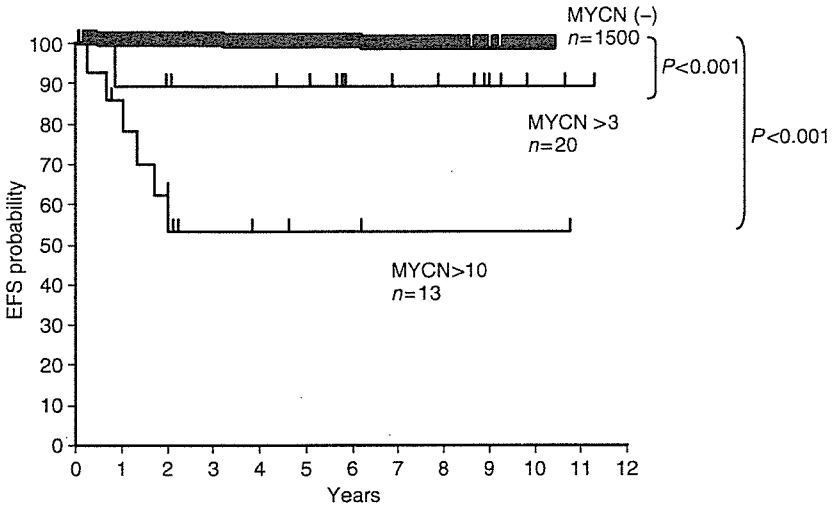

Figure 1 Four-year event-free survival of neuroblastoma infants detected by mass screening based on *MYCN* amplification. The curve was generated with the Kaplan and Meier product limit method. The 4-year OS rate was 99% for patients without MNA, 89% for patients with amplification from three to nine copies, and 53% for patients with more than 10 copies ($P<0.001$).

MNA, it is necessary to establish and perform the appropriate treatment, including not only surgical resection but also chemotherapy.

MYCN amplification was strongly and inversely correlated with the prognosis in infantile cases, although the frequency of MNA in the cases discovered through the MSPN was small (2.2%). Prediction of the presence of MNA in the tumour based on urinary levels of HVA and VMA and stage of the tumour was difficult in the cases we encountered. Our results demonstrate that evaluation of MNA is important for the selection of appropriate treatment for infantile NB.

ACKNOWLEDGEMENTS

The authors gratefully thank many pediatric oncologists and pediatric surgeons in Japan for providing us the important clinical data of patients study. This study was supported in part by grants for cancer and mass-screening research from the Kyoto Prefectural Govement and the Children's Cancer Association of Japan. This study was also supported in part by Grant-in-Aid for Scientific Research (16-Kodomo-012) from the Ministry of Health, Labour, and Welfare of the Government of Japan.

REFERENCES

Berthold F, Hero B (2000) Neuroblastoma: current drug therapy recommendations as part of the total treatment approach. *Drugs* **59:** 1261–1277

Brodeur GM (2003) Neuroblastoma: biological insights into a clinical enigma. *Nat Rev Cancer* **3:** 203–216

Brodeur GM, Pritchrd J, Berthold F, Carlsen NL, Castel V, Castelberry RP, De Bernardi B, Evans AE, Favrot M, Hedborg F (1993) Revisions of the international criteria for neuroblastoma diagnosis, staging, and response to treatment. *J Clin Oncol* **11:** 1466–1477

Brodeur GM, Seeger RC, Schwab M, Varmus HE, Bishop JM (1984) Amplification of *N-myc* in untreated human neuroblastomas correlates with advanced disease stage. *Science* **224:** 1121–1124

Cohn SL, Look AT, Joshi VV, Holbrook T, Salwen H, Chagnovich D, Chesler L, Rowe ST, Valentine MB, Komuro H (1995) Lack of correlation of *N-myc* gene amplification with prognosis in localized neuroblastoma: A Pediatric Oncology Group study. *Cancer Res* **55:** 721–726

D'angio GJ, Evans AE, Koop CE (1971) Special pattern of widespread neuroblastoma with a favorable prognosis. *Lancet* **1:** 1046–1049

Evans AE, D'angio GJ, Randolph J (1971) A proposal staging for children with neuroblastoma. *Cancer* **27:** 374–378

Hachitanda Y, Ishimoto K, Hata J, Shimada H (1994) One hundred neuroblastomas detected through a mass screening system in Japan. *Cancer* **74:** 3223–3226

Honjyo S, Doran H, Stiler C, Ajiki W, Tsukuma H, Oshima A, Coleman MP (2003) Neuroblastoma trends in Osaka, Japan, and Great Britain 1970–1994, in relation to screening. *Int J Cancer* **103:** 538–543

Ikeda H, Iehara T, Tsuchida Y, Kaneko M, Hata J, Naito H, Iwafuchi M, Ohnuma N, Mugishima H, Toyoda Y, Hamazaki M, Mimaya J, Kondo S, Kawa K, Okada A, Hiyama E, Suita S, Takamatsu H (2002) Experience with International Neuroblastoma Staging System and Pathology Classification. *Br J Cancer* **86:** 1110–1116

Kaneko M, Tsuchida Y, Mugishima H, Ohnuma N, Yamamoto K, Kawa K, Iwafuchi M, Sawada T, Suita S (2002) Intensified chemotherapy increases the survival rates in patients with stage 4 neuroblastoma with *MYCN* amplification. *J Pediatr Hematol Oncol* **24:** 613–621

Kawa K, Ohnuma N, Kaneko M, Yamamoto K, Etoh T, Mugishima H, Ohhira M, Yokoyama J, Bessho F, Honna T, Yoshizawa J, Nakada K, Iwafuchi M, Nozaki T, Mimaya J, Sawada T, Nakamura T, Miyata H, Yamato K, Tsuchida Y (1999) Long-term survivors of advanced neuroblastoma with *MYCN* amplification: A report of 19 patients surviving disease-free for more than 66 months. *J Clin Oncol* **17:** 3216–3220

Kerbl R, Urban CE, Ambros IM, Dornbusch HJ, Schwinger W, Lackner H, Ladenstein R, Strenger V, Gadner H, Ambros PF (2003) Neuroblastoma mass screening in late infancy: insights into the biology of neuroblastic tumors. *J Clin Oncol* **21:** 4228–4234

Kusafuka T, Nagahara N, Oue T, Imura K, Nakamura T, Kobayashi Y, Komoto Y, Fukuzawa M, Okada A, Nakayama M (1995) Unfavorable DNA ploidy and Ha-ras p21 findings in neuroblastomas detected through mass screening. *Cancer* **76:** 695–699

Look AT, Hayes FA, Shuster JJ, Douglass EC, Castleberry RP, Bowman LC, Smith EI, Brodeur GM (1991) Clinical relevance of tumor cell ploidy and N-myc gene amplification in childhood neuroblastoma: a pediatric oncology group study. *J Clin Oncol* **9:** 581–591

Mathew P, Valentine MB, Bowman LC, Rowe ST, Nash MB, Valentine VA, Cohn SL, Castleberry RP, Brodeur GM, Look AT (2001) Detection of *MYCN* gene amplification in neuroblastoma by fluorescence *in situ* hybridization: a pediatric oncology group study. *Neoplasia* **3:** 105–109

Matsumura T, Michon J (2000) Treatment of localized neuroblastoma. In *Neuroblastoma*, Brodeur GM, Sawada T, Tsuchida Y and Voute PA (eds) pp 403–415. Amsterdam: Elsevier

Matsunaga T, Shirasawa H, Hishiki T, Yoshida H, Kouchi K, Ohtsuka Y, Kawamura K, Etoh T, Ohnuma N (2000) Enhanced expression of *N-myc* messenger RNA in neuroblastomas found by mass screening. *Clin Cancer Res* **6:** 3199–3204

Perez CA, Matthy KK, Atkinsin JB, Seeger RC, Shimada H, Haase GM, Stram DO, Gerbing RB, Lukens JN (2000) Biologic variable in the outcome of stages I and II neuroblastoma treated with surgery as primary therapy: a Children's Cancer Group study. *J Clin Oncol* **18:** 18–26

Rubie H, Hartmann O, Michon J, Frappaz D, Coze C, Chastagner P, Baranzelli MC, Plantaz D, Avet-Loiseau H, Benard J, Delattre O, Favrot M, Peyroulet MC, Thyss A, Perel Y, Bergeron C, Courbon-Collet B, Vannier JP, Lemerle J, Sommelet D (1997) *N-myc* gene amplification is a major prognostic factor in localized neuroblastoma: Results of the French NBL 90 study. *J Clin Oncol* **15:** 1171–1182

Sawada T (1988) Laboratory techniques and neuroblastoma screening. *Lancet* **2:** 1134–1135

Sawada T, Hirayama M, Nakata T, Takeda T, Takasugi N, Mori T, Maeda K, Koide R, Hanawa Y, Tsunoda A (1984) Mass screening for neuroblastoma in infants in Japan. Interim report of a mass screening group. *Lancet* **2:** 271–273

Sawada T, Nishi M, Takeda T, Iehara T (1998) Mass screening for neuroblastoma in Japan. *Med Pediatr Oncol* **31:** 429–434

Spitz R, Hero B, Skowron M, Ernestus K, Berthold F (2004) *MYCN*-status in neuroblastoma: characteristics of tumours showing amplification, gain, and non-amplification. *Eur J Cancer* **40:** 2753–2759

Tajiri T, Suita S, Sera Y, Takamatsu H, Mizote H, Nagasaki A, Kurosaki N, Handa N, Hara T, Okamura J, Miyazaki S, Sugimoto T, Kawakami K, Eguchi H, Tsuneyoshi M (2001) Clinical and Biologic Characteristics for recurring neuroblastoma at mass screening cases in Japan. *Cancer* **92:** 349–353

Tanaka T, Sugimoto T, Sawada T (1998) Prognostic discrimination among neuroblastomas according to *Ha-ras/trk A* gene expression: a comparison of the profiles of neuroblastomas detected clinically and those detected through mass screening. *Cancer* **83:** 1626–1633

Tonini GP, BOni L, Pession A, Rogers D, Iolascon A, Basso G, Cordero di Montezemolo L, Casale F, Pession A, Perri P, Mazzocco K, Scaruffi P, Lo Cunsolo C, Marchese N, Milanaccio C, Conte M, Bruzzi P, De Bernardi B (1997) *MYCN* oncogene amplification in neuroblastoma is associated with prognosis, except in stage 4s: The Italian experience with 295 children. *J Clin Oncol* **15:** 85–93

Woods WG, Gao RN, Shuster JJ, Robison LL, Bernstein M, Weitzman S, Bunin G, Levy I, Brossard J, Dougherty G, Tuchman M, Lemieux B (2002) Screening of infants and mortality due to neuroblastoma. *N Engl J Med* **346:** 1041–1046

Yamamoto K, Hanada R, Kikuchi A, Ichikawa M, Aihara T, Oguma E, Moritani T, Shimanuki Y, Tanimura M, Hayashi Y (1998) Spontaneous regression of localized neuroblastoma detected by mass screening. *J Clin Oncol* **16:** 1265–1269

Yamamoto K, Ohta S, Ito E, Hayashi Y, Asami T, Mabuchi O, Higashigawa M, Tanimura M (2002) Marginal decrease in mortality and marked increase in incidence as result of neuroblastoma screening at 6 months of age: Cohort study in seven prefectures in Japan. *J Clin Oncol* **20:** 1209–1214

Appendix A1

Participating institutions main investigators

Gunma Children's Medical Center, Gunma (Tsuchida Y, Kuroiwa M); Osaka University, Osaka (Fukuzawa M, Kusafuka T, Yoneda M); Osaka Medical Center for Maternal and Child Health, Osaka (Kawa K, Inoue M, Oue T); Kumamoto University, Kumamoto (Sera Y, Inomata Y); Tokusima University, Tokushima (Takahara H); Hyogo Children's Hospital, Hyogo (Misu H); Kyushu University, Fukuoka (Suita S, Tajiri T); Keio University, Tokyo (Yokoyama J, Morikawa Y); National Sapporo Hospital, Hokkaido (Hatae Y, Naito H); National Center for Child Health and Development (Honna T). National Nagoya Hospital, Aichi (Horibe K); Tohoku University, Miyagi (Hayashi Y); Nihon University, Tokyo (Mugishima H, Koshinaga T); Dokkyo University, Saitama (Ikeda H).

Anal Bioanal Chem (2006) 385: 814–820
DOI 10.1007/s00216-006-0459-5

ORIGINAL PAPER

Tomomi Hasegawa · Kastuya Wada · Eiso Hiyama · Tsutomu Masujima

Pretreatment and one-shot separating analysis of whole catecholamine metabolites in plasma by using LC/MS

Received: 13 February 2006 / Revised: 7 March 2006 / Accepted: 30 March 2006 / Published online: 7 June 2006

Abstract Catecholamines are biogenic amines that play an important role in the nervous system. Some catecholamines have been used as tumor makers of phenochromocytoma, paraganglioma and neuroblastoma. The analysis of total catecholamine metabolites should be useful for one-shot screening of multiple aspects of diseases; however, it is difficult to do this, because the catecholamine metabolites are divided into three groups: five amines, one amino acid and three carbonic acids. Catecholamines and small molecules were separated from plasma proteins by an internal-surface reversed-phase column (protein-coated octadeyclsilica column) and were analyzed by liquid chromatography (LC)/mass spectrometry (MS) using electrospray ionization time-of-flight MS. Using a reversed-phase column and hydrophilic mobile phases, we succeeded in the separation of nine catecholamines, all of which had similar structures. These nine substances were eluted in the following order: norepinephrine, epinephrine, normetanephrine, dopamine, metanephrine, 3,4-dihydroxyphenylalanine, vanillomandelic acid, 3,4-dihydroxyphenylacetic acid and homovanillic acid. The reproducibility of this method was acceptable. The highest coefficient of variation was 7.4%. In addition, various types of compounds were separated from and detected in plasma proteins by applying LC/MS. The plasma direct injection method, which uses an internal-surface reversed-phase column and an ion-pair reagent, allowed us to separate small molecules from plasma proteins. MS detected some compounds that high-performance LC could not succeed in separating and detecting with UV detection. We think that the method can be applied to find new markers in neuroblastoma, by comparing the plasma of patients with that of normal infants. The method can be also used to help in making a diagnosis of other diseases and finding their new makers.

T. Hasegawa · K. Wada · E. Hiyama · T. Masujima (✉)
Graduate School of Biomedical Science, Hiroshima University,
1-2-3 Kasumi, Minami-ku,
Hiroshima, 732-8551, Hiroshima, Japan
e-mail: tsutomu@hiroshima-u.ac.jp
Tel.: +81-82-2575300
Fax: +81-82-2575304

Keywords Neuroblastoma · Catecholamine · Internal-surface reversed-phase column · Liquid chromatography/mass spectrometry

Abbreviations BSA: Bovine serum albumin · DOPA: 3,4-Dihydroxyphenylalanine · DOPAC: 3,4-Dihydroxyphenylacetic acid · ESI: Electrospray ionization · HPLC: High-performance liquid chromatography · HVA: Homovanillic acid · LC: Liquid chromatography · MS: Mass spectrometry · ODS: Octadecylsilica · VMA: Vanillomandelic acid

Introduction

Neuroblastoma is a malignant tumor especially found in infants. The frequency of the incidence is the second highest after that of leukemia. Because of its high frequency and the possibility of curing the disease with early detection, a nationwide neonatal mass screening at 6 months of age was conducted in Japan between 1985 and 2004. Infants with neuroblastoma produce an excess of catecholamines compared with normal infants [1]. Therefore, a considerable amount of vanillomandelic acid (VMA) and homovanillic acid (HVA), the final metabolites of catecholamines, is excreted in the urine [2–7]. The present mass screening observed an increase of the final metabolites by high-performance liquid chromatography (HPLC) [8, 9]; however, this screening method had problems with both the accuracy of metabolite measurement and the determination of a definitive cutoff value. The committee of the Ministry of Health, Labour and Welfare in Japan reached the conclusion that the screening has no effect on mortality from neuroblastoma, and thus it was suspended [10, 11]. Contrary to the negative opinions, some believe that the mass screening actually helped reduce mortality due to neuroblastoma. This disease is still a convalescent unsatisfactory disease and, therefore, mass screening is vital to a reduction of the mortality due to infantile cancers [12–14]. In order to restart the mass screening, the current method, which targets only the final

substances (VMA and HVA) and considers metabolic substances of catecholamine to be insignificant, needed to be reexamined. We analyzed all metabolic substances of catecholamine, including metabolic by-products, and set up an analytical method using liquid chromatography (LC)/mass spectrometry (MS). Urine is the correct sample for the screening, posing the least burden and risk to infants and their parents; however, urine does not contain all of the compounds of the human body and there is also a problem with the stability of components generated by contamination. Blood, on the other hand, contains all of the compounds of the human body; thus, we established a test method for analysis of plasma.

In the plasma, small molecules unite with plasma proteins, especially albumin. For the analysis of small molecules in the plasma, these small molecules needed to be separated from plasma proteins. For the separation, we employed a direct plasma injection analysis, which uses an internal-surface reversed-phase column. Figure 1 shows the characteristics of the column. The outside surface of porous resins was coated with bovine serum albumin (BSA), so that the column did not adsorb the plasma proteins, but still had the reversed-phase characteristics for small molecules. The internal-surface reversed-phase column was selected as a precolumn for the deproteinization and trapping of small molecules [15, 16].

In the human body, catecholamines are formed by the following sequence of reactions: tyrosine→3,4-dihydroxyphenylalanine (DOPA)→dopamine→norepinephrine→epinephrine. They all have physiological activity. After they have performed their roles, DOPA is metabolized and becomes HVA via 3,4-dihydroxyphenylacetic acid (DOPAC). Dopamine also changes into HVA. Norepinephrine transforms into normetanephrine, and epinephrine becomes metanephrine. They then both transform into VMA. These reactions are catalyzed by the following enzymes: tyrosine hydroxylase, DOPA decarboxylase, dopamine-β-hydroxylase, phenylethanolamine-*N*-methyltransferase, catechol-*O*-methyltransferase, and monoamine oxidase. Finally HVA and VMA are excreted in the urine (Fig. 2).

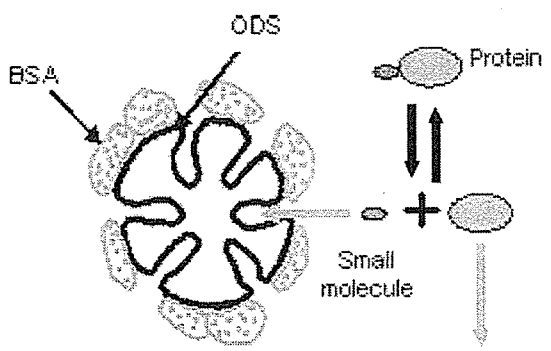

Fig. 1 The characteristics of the internal-surface reversed-phase column. This column was selected as a precolumn for the deproteinization and trapping of small molecules. *BSA* bovine serum albumin, *ODS* octadecylsilica

Materials and methods

Chemicals

DOPA, dopamine, DOPAC, epinephrine, normetanephrine, metanephrine, HVA, VMA and formic acid were obtained from Sigma. Norepinephrine was from Fluka. Methanol, acetonitrile, ammonia solution, ammonium hydrogencarbonate and pentadecafluorooctanoic acid [$CF_3(CF_2)_6$ COOH] were purchased from Kanto Chemical. Trifluoroacetic acid (CF_3COOH), pentafluoropropionic acid (CF_3CF_2COOH) and heptafluorobutyric acid [$CF_3(CF_2)_2$ COOH] were obtained from Aldrich. Nonafluorovaleric acid [$CF_3(CF_2)_3COOH$] was from Tokyo Kasei Kogyo. Methanol and acetonitrile were HPLC grade, and all other reagents were analytical grade. Water was deionized and purifed by a Milli-Q Academic A10 purification system from Millipore.

Sample preparation

Catecholamine metabolites were dissolved in water at a concentration of 1 mg/mL and mixed in one solution to a final concentration of 100 μg/mL to form a standard solution. The standard solution was diluted with fetal bovine serum or human plasma to 10 μg/mL and was used as sample-spiked plasma.

Instrumentation

The HPLC-UV system was a Gulliver series system from JASCO, consisting of a DG-980-50 3 line degasser, an LG-1580-02 ternary gradient unit, a PU-980 Intelligent HPLC pump and a UV-970 Intelligent UV/vis detector. Pretreatment was performed by using the internal-surface reversed-phase column (TSK precolumn BSA-ODS:TOSOH) and a column-packed anion-exchange resin (TOYOPEARL QAE-550:TOSOH). The analysis column was an L-column ODS (150 mm×4.6 mm, 5 μm) from CERI. MS analysis was performed using a Mariner electrospray ionization (ESI) time-of-flight mass spectrometer from Applied Biosystems.

Chromatographic conditions

Mobile phases for the pretreatment column were water containing 1% of formic acid (solvent A) and 200 mM ammonium hydrogencarbonate buffer/acetonitrile (5:95 v/v) (solvent B). The internal-surface reversed-phase column was equilibrated with solvent A at a flow rate of 0.5 mL/min, and samples were injected into the HPLC system. Following the removal of plasma proteins and other hydrophilic compounds, the mobile phase was changed to solvent B by switching a six-port valve. Catecholamine metabolites and hydrophobic compounds were eluted, and the fractions were collected. Then, the fractions were evaporated. The residue

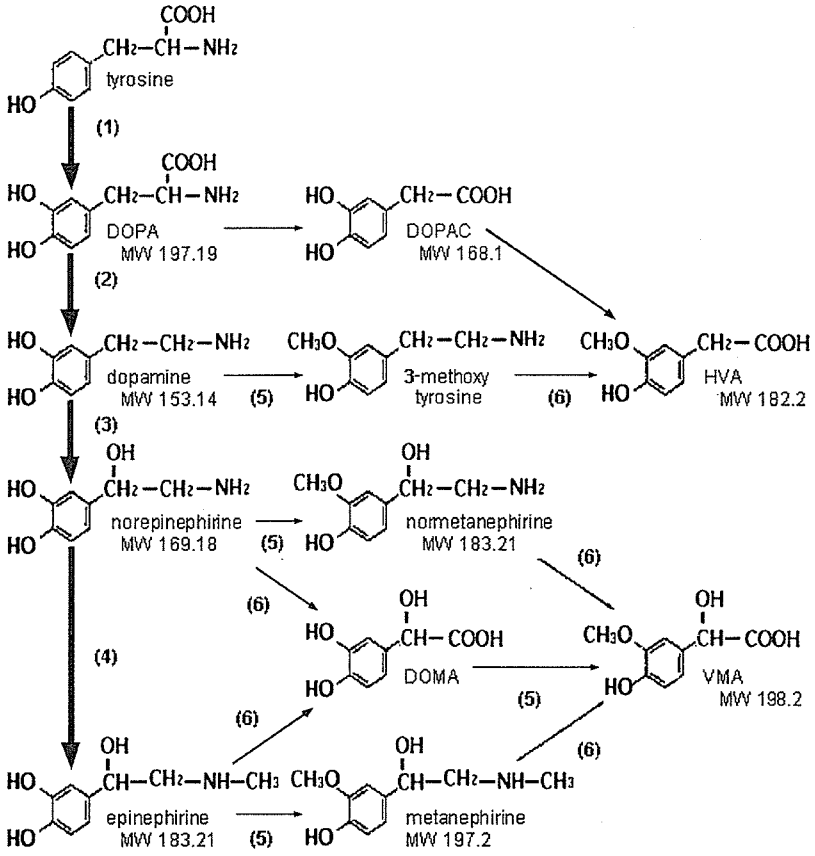

Fig. 2 The pathway of synthesis and metabolites of catecholamines: *1* tyrosine hydroxylase, *2* 3,4-dihydroxyphenylalanine (*DOPA*) decarboxylase, *3* dopamine-β-hydroxylase, *4* phenylethanolamine-*N*-methyltransferase, *5* catechol-*O*-methyltransferase, *6* monoamine oxidase. *DOPAC* 3,4-dihydroxyphenylacetic acid, *HVA* homovanillic acid, *VMA* vanillomandelic acid

was dissolved in 100 µL of the mobile phase, and 20 µL was injected into the LC/MS system. The two mobile phases used for the analysis of these treated samples were solvent A and methanol containing 1% of formic acid (solvent C). Separation was conducted at a flow rate of 0.2 mL/min. For the separation of amines, the concentration of solvent C was 5% for the first 18 min. In order to elute VMA, DOPAC and HVA the concentration of solvent C was raised to 45% for the next 12 min. The UV detector was set to monitor 280 nm. The mass spectrometer was used in the positive-ion ESI mode.

Results and discussion

Separation of catecholamine metabolites

We developed a method for the HPLC separation of catecholamine metabolites. The catecholamine metabolites were divided into two groups: five amines and one amino acid, and three carbonic acids. In order to separate the five amines and one amino acid, the structures of which were similar, the hydrophilic mobile phase needed to be used. In this case, we used 1% of formic acid/methanol (5:95 v/v) and achieved a good separation. Figure 3 shows the LC and MS chromatograms. The elution order was norepinephrine, epinephrine, normetanephrine, dopamine, metanephrine and DOPA. The peaks of norepinephrine were at *m/z* 152 ($[M+H-H_2O]^+$) and *m/z* 170 ($[M+H]^+$). Epinephrine was detected at *m/z*184 ($[M+H]^+$), normetanephrine was detected at *m/z* 166 ($[M+H-H_2O]^+$) and *m/z* 184 ($[M+H]^+$), dopamine was detected at *m/z* 154 ($[M+H]^+$), and metanephrine and DOPA were detected at *m/z* 180 ($[M+H-H_2O]^+$) and *m/z* 198 ($[M+H]^+$).

DOPAC, HVA and VMA have a strong affinity with ODS. To accelerate the elution of these three substances, the concentration of the organic mobile phase was raised from 5 to 45%. As a result, all procedures were carried out within 60 min. The elution order of carbonic acids was VMA, DOPAC and HVA (Fig. 4). The peaks of DOPAC were at *m/z* 169 ($[M+H]^+$), *m/z* 186 ($[M+NH_4]^+$) and *m/z* 191 ($[M+Na]^+$). HVA was detected at *m/z* 183 ($[M+H]^+$), *m/z* 200 ($[M+NH_4]^+$) and *m/z* 205 ($[M+Na]^+$). No peak was found for VMA. It is suspected that because VMA has a hydroxyl group close to the carboxyl group, the pK_a is lower compared with that of other carbonic acids. Thus VMA could not be ionized well with the positive ESI mode.

By trapping the catecholamine metabolites on the internal-surface reversed-phase column, we separated catecholamine metabolites and small molecules from plasma proteins. Plasma proteins ran through the column without being trapped, because of the size exclusion and the coated BSA. We set the elution time of proteins by the HPLC-UV and Lowry method (absorbance of 700 nm). At a flow rate of 0.5 mL/min and 100 µL of sample volume, plasma proteins were eluted from the column within 3 min (Fig. 4a,b). Under these conditions the internal-surface ODS did not hold catecholamine metabolites well enough,

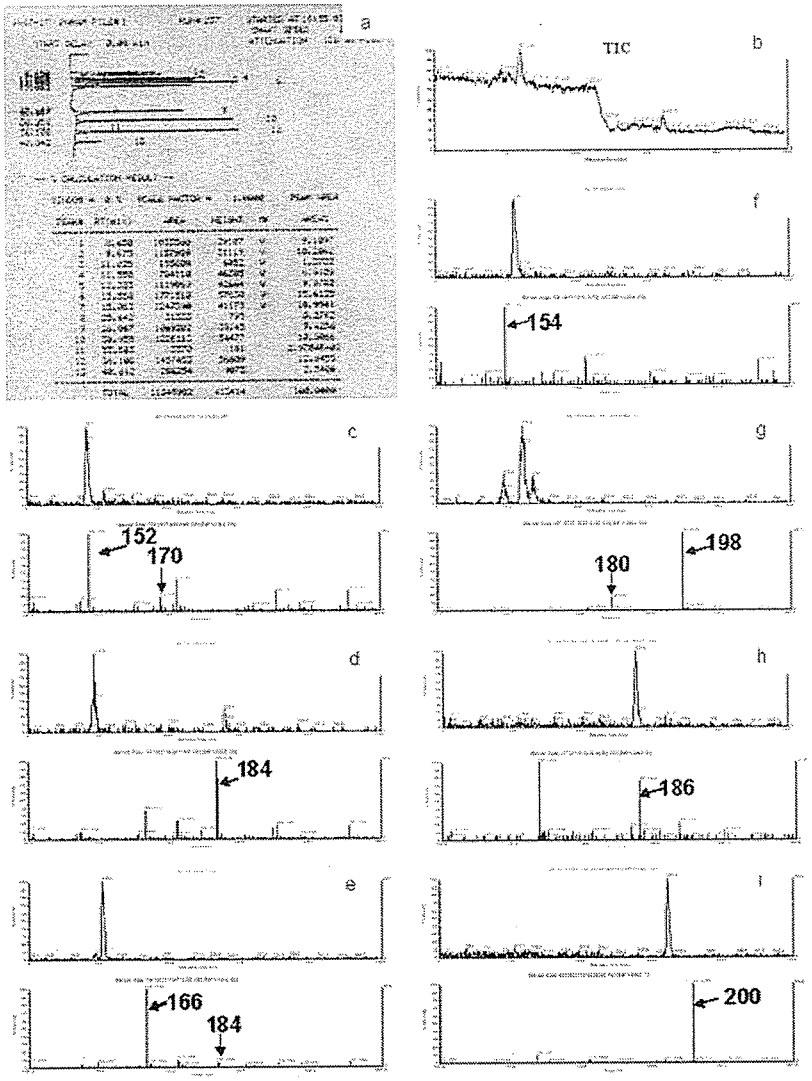

Fig. 3 **a** The liquid chromatography (*LC*) chromatogram. The elution order was norepinephrine, epinephrine, normetanephrine, dopamine, metanephrine, DOPA, VMA, DOPAC and HVA. Flow rate 0.2 mL/min, sample concentration 10 μg/mL, sample volume 20 μL, detection 280 nm. **b** Mass spectrometry (*MS*) total ion chromatogram (*TIC*) (electrospray ionization time-of-flight, *ESI-TOF*, MS; positive mode). **c** Norepinephrine *m/z* 152([M+H−H_2O]$^+$), *m/z* 170 ([M+H]$^+$). **d** Epinephrine *m/z* 184 ([M+H]$^+$). **e** Normetanephrine *m/z* 166 ([M+H−H_2O]$^+$), *m/z* 184 ([M+H]$^+$). **f** Dopamine *m/z* 154 ([M+H]$^+$). **g** Metanephrine, DOPA *m/z* 180 ([M+H−H_2O]$^+$), *m/z* 198 ([M+H]$^+$). **h** DOPAC *m/z* 169 [M+H]$^+$, *m/z* 186 [M+NH_4]$^+$, *m/z* 191 [M+Na]$^+$. **i** HVA *m/z* 183 [M+H]$^+$, *m/z* 200 [M+NH_4]$^+$, *m/z* 205 [M+Na]$^+$

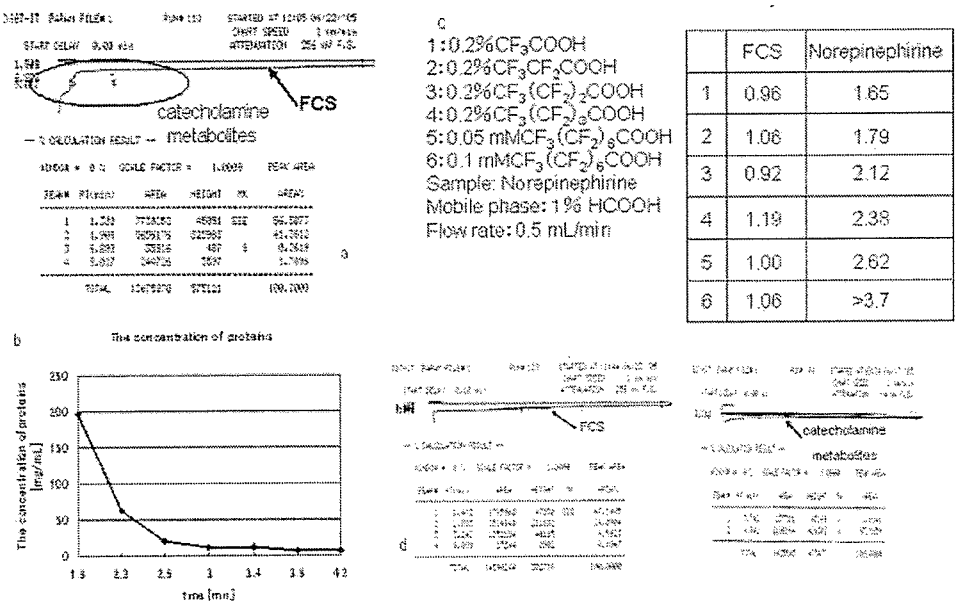

	FCS	Norepinephrine
1	0.96	1.65
2	1.06	1.79
3	0.92	2.12
4	1.19	2.38
5	1.00	2.62
6	1.06	>3.7

Fig. 4 **a** LC chromatogram of sample-spiked fetal calf serum (*FCS*). ODS did not hold catecholamine metabolites. **b** Change of protein concentration. Plasma proteins ran down within 3 min. **c** The effect of the ion-pair reagent: 0.1 mM pentadecafluorooctanoic acid/1% formic acid gave good separation. **d** *A* Injection→3 min; *B* after column switching

Table 1 The evaluation of reproducibility, recovery and detection limit (n=5)

	Recovery (%)	Mean	Standard deviation	Coefficent of variation (%)	Detection limit: signal-to-noise ratio of 3 (μg/mL)
Norepinephrine	94.1	305,000	21,400	7.0	1
Epinephrine	94.1	363,000	27,700	7.6	1
Normetanephrine	97.9	294,000	7,900	2.7	1
Dopamine	93.3	341,000	12,300	3.6	1
Metanephrine	93.3	357,000	18,400	5.2	1
3,4-Dihydroxyphenylalanine	94.0	323,000	7,300	2.6	1.5
Tyrosine	97.4	207,000	7,200	3.5	1
Vanillomandelic acid	87.0	145,000	11,000	7.4	–
3,4-Dihydroxyphenylacetic acid	97.7	350,000	11,000	3.1	1.5
Homovanillic acid	98.0	435,000	26,000	6.0	1

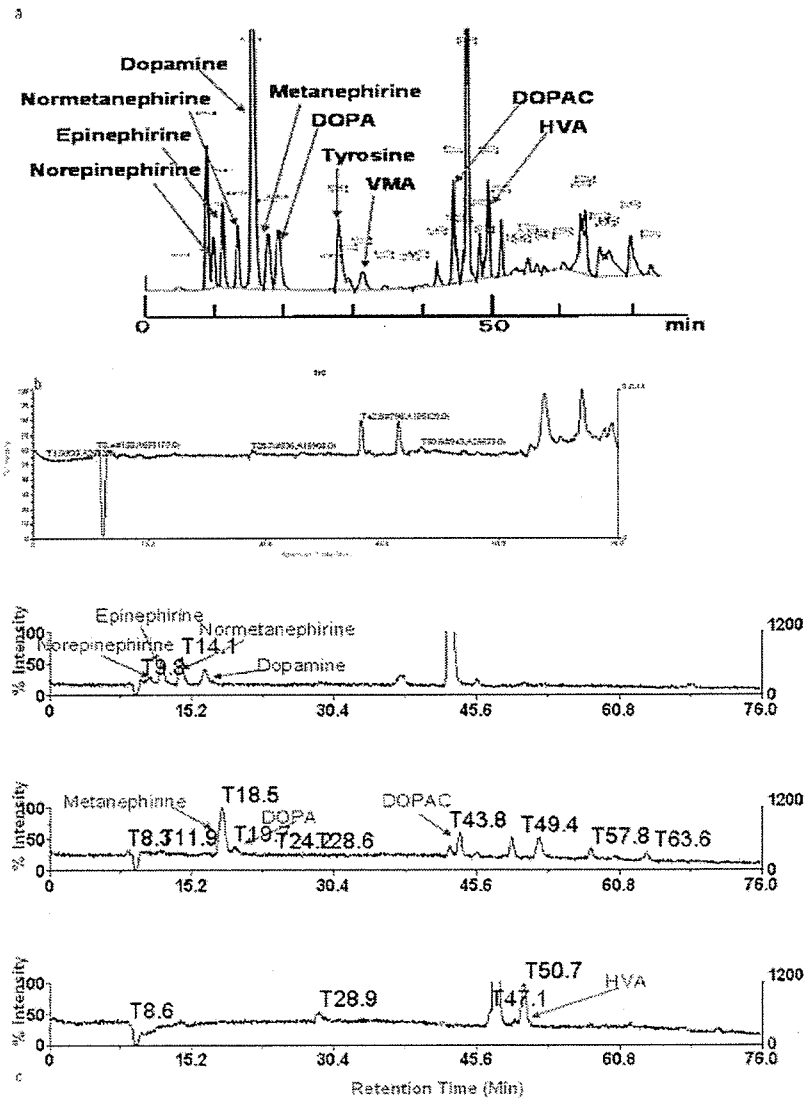

Fig. 5 **a** The LC chromatogram of sample-spiked plasma. We investigated a variety of compounds in plasma and achieved a clear separation by high-performance LC-UV detection for standard compounds. **b** MS-TIC (ESI-TOF/MS; positive mode). **c** The MS chromatogram. Standard compounds were detected by their peaks

time	m/z					
9.5	147	149	163	167	172	189
9.8	177					
9.9	266	267	268			
9.8	271					
9.7	266	297				
9.9	172					
9.9	208	234	264	279	280	
10.1	175					
10.2	182	183	227	228	229	
14	204					
15	235					
16	137					
17.5	150	151				
28.9	183					
37.5	166					
41.9	195					
42.5	166	167	168	169		
43.2	191					
43.8	265					
43.9	163	180	282			

time	m/z				
44.8	256				
45.7	167	184			
45.9	168				
46.1	181				
46.7	283	300	301		
47	239				
47.6	188	205	206	207	
49.4	180	181	196		
49.5	285				
49.7	222				
50.4	222				
50.7	183	200	201		
50.8	282				
52.3	166	167	277		
52.8	153				
53	256				
53.2	172				
53.3	180				
55.1	181				
56	291				

time	m/z							
56.1	239							
57.8	163	180						
59	190							
60.1	191							
60.9	267	268						
63.3	182							
63.6	191							
63.7	209							
64.5	223	224	241	242	263			
65.2	268							
65.5	264	249	250	251	271	272	273	
66.7	266	267	268					
67.6	268	267						
68.1	294							
68.8	269	270						
69.9	280							
70.1	299							
70.8	284							
71.3	279	280	291					
72.3	252							

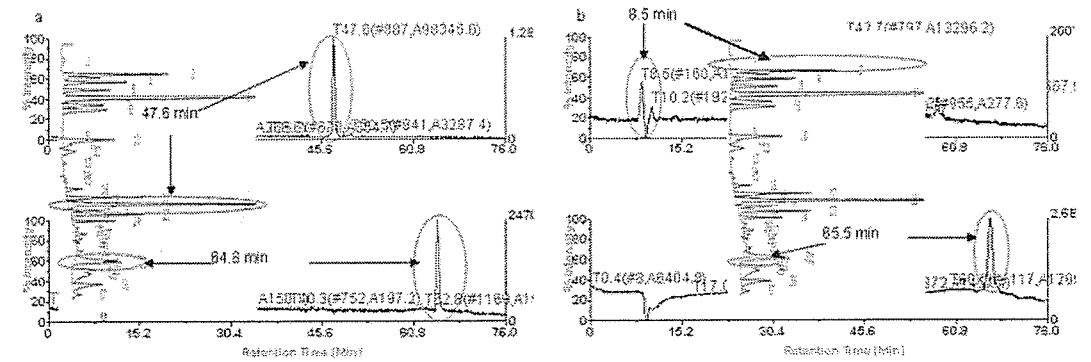

Fig. 6 The ion peaks without catecholamine metabolites detected by ESI-TOF/MS; positive mode. **a** Two peaks detected by both HPLC-UV and MS. **b** Two peaks detected only by MS

because they were ionized. In order to increase the affinity of ODS, we used a volatile ion-pair reagent [17, 18]. With the reagent, trifluoroacetic acid, pentafluoropropionic acid, heptafluorobutyric acid, nonafluorovaleric acid and pentadecafluorooctanoic acid were tested (Fig. 4c). We accomplished a good separation using 0.1 mM pentadecafluorooctanoic acid/1% formic acid (Fig. 4d). With this mobile phase, the ion-pair reagent was not removed by evaporation. We placed a column-packed strong anion-exchange resin between the switching six-port valve and the UV detector. As a result, the ion-pair reagent was adsorbed to anion-exchange resin and removed.

Recovery, reproducibility and detection limit

The recovery, reproducibility and detection limit of this method are summarized in Table 1. The sample concentration was 10 μg/mL and the volume was 100 μL. The evaluation was done based on the peak area of the chromatogram. The recovery for VMA was rather low owing to weak retention, but for the other compounds it was more than 90%. The reproducibility for norepinephrine, epinephrine and VMA, which are retained weakly in the pretreatment column, were rather high, but for the other compounds it was within an acceptable level of less than 6% for the coefficient of variation. Since the retention times of these compounds fluctuate in the pretreatment process depending on the presaturated ion-pair concentration, the dispersion of the reproducibility for the compounds seemed to be caused by the concentration of the ion-pair reagent in the internal-surface reversed-phase column. The detection limit at a signal-to-noise ratio of 3 was around 1–1.5 μg/mL. In order to improve the sensitivity, micro-LC/MS and Quadruple mass filter detection can be adopted.

Analysis of the total catecholamine metabolites in plasma

A 100-μL aliquot of sample-spiked plasma was analyzed by the present method. Figure 5 shows the results. We investigated a variety of compounds in plasma and achieved a clear separation by HPLC as shown by UV and MS detection. Figure 6 shows the ion peaks without catecholamine metabolites. Some of the peaks were identified by both HPLC-UV and MS (Fig. 6a), and the rest of them were detected only by MS, indicating that they had no significant UV absorption (Fig. 6b).

Conclusion

For analysis of the metabolic process of catecholamines released from cells such as nerve cells, we established an analytical method for all catecholamine metabolites using a preconcentration column and LC/MS. We succeeded in separating catecholamine metabolites and hydrophobic compounds from plasma proteins in a single separation process by using the internal-surface reversed-phase column and an ion-pair reagent in the pretreatment process. In addition, MS was able to identify some compounds that could not be separated or detected by HPLC. The recovery weas almost 90%, the reproducibility had a coefficient of variation of less than 7% and the detection limit at a signal-to-noise ratio of 3 was around 1–1.5 μg/mL. This method can be applied to help find new markers in neuroblastoma, by comparing the plasma of patients with that of normal infants. The method can also be used to make a diagnosis of other diseases or to find their new markers.

Acknowledgement This work was partly supported by Grants-in-Aid for Scientific Research from the Ministry of Education, Science, Sports, and Culture of Japan.

References

1. Mason GA, Hart-Mercer J, Millar EJ, Strang LB, Wynne NA (1957) Lancet 270(6990):322–325
2. Gitlow SE, Bertani LM, Rausen A, Gribetz D, Dziedzic SW (1970) Cancer 25(6):1377–1383
3. Liebner EJ, Rosenthal IM (1973) Cancer 32(3):623–633
4. Voorhess ML, Gardner LI (1961) Lancet I 1288
5. Kontras SB (1962) Cancer 15:978–986
6. Williams CM, Greer M (1963) JAMA 183:836–840
7. Sourkes TL, Denton RL, Murphy GF, Chavez B, Saint Cyr S (1963) Pediatrics 31:660–668
8. Sato Y, Hanai J, Takasugi N, Takeda T (1986) Tohoku J Exp Med 150(2):169–174
9. Sawada T (1988) Lancet Nov 12 2(8620):1134–1135
10. Woods WG, Tuchman M, Robison LL, Bernstein M, Leclerc J-M, Brisson LC et al (1996) Lancet 348(9043):1682–1687
11. Schilling FH, Spix C, Berthold F, Erttmann R, Fehse N, Hero, B et al (2002) N Engl J Med 346(14):1047–1053
12. Nishi M, Takeda T, Hatae Y, Hanai J, Fujita K, Ichimiya H, Tanaka T (2002) J Exp Clin Cancer Res 21(1):73–78
13. Yamamoto K, Ohta S, Ito E, Hayashi Y, Asami T, Mabuchi O et al (2002) J Clin Oncol 20(5):1209–1214
14. Tsuchida Y, Ikeda H, Shitara T, Tanimura M (2000) Med Pediatr Oncol 34(1):80–81
15. Hisanobu Y, Keiko T, Ikue M, Tutomu M, Hideo I (1983) Jpn J Clin Chem 12(4):312–218
16. Ikue M, Tutomu M, Hisanobu Y, Hideo I (1983) Jpn J Clin Chem 12(4):312–218
17. Fuh M-R, Haung C-H, Lin S-L, Pan WHT (2004) J Chromatogr A 1031(1–2):197–201
18. Qu J, Wang Y, Luo G, Wu Z, Yang C (2002) Anal Chem 74 (9):2034–2040

For reprint orders, please contact:
reprints@futuremedicine.com

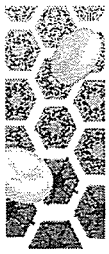

Videovisualization of dynamic cell responses and its molecular analysis for nanomedicine

Tsutomu Masujima†, Naohiro Tsuyama & Tomomi Hasegawa

†Author for correspondence
Analytical Molecular Medicine and Devices Laboratory, Graduate School of Medical Sciences, Hiroshima University, 1-2-3 Kasumi, Minami-ku, Hiroshima 734–8551, Japan
Tel.: +81 82 257 5301;
Fax: +81 82 257 5304;
E-mail: tsutomu@hiroshima-u.ac.jp

This report proposes and reviews a new approach that provides a more straightforward methodology for visualizing and determining molecular mechanisms as they occur within cells. A direct observation of the dynamic behavior of cells using a video microscope shows unexpected but very rational behavior that challenges us to elucidate its molecular mechanism. Since mass spectrometry is a rapid and sensitive tool for molecular analysis, single-cell matrix-assisted laser desorption-ionization time of flight mass spectrometry is useful and a morphological and molecular analysis combined method called video-mass-scope is also proposed. For analysis of the function of new molecules, single molecular imaging should be straightforward and the dynamic image of molecular movement or transport, called nanokinetics, is also necessary for the application to nanomedicine. Various research examples, based mainly on biological self-defense or secretion processes, are reviewed. The combination of these analytical techniques will enable us to understand the dynamic molecular mechanisms of cells and this knowledge could be applied to nanomedicine in the future.

For the development of molecular-based medicine, molecular analyses of biological systems are essential. Conventional biochemical molecular analyses require a large number of cells. Therefore, the conclusions are, in fact, an average of all the cells involved. However, when we observed cell behavior over time, we learned that even cells of the same type do not have identical responses. Cells are independent to some extent and their behaviors are task-oriented and unexpected. Direct observation can be more valuable than mere textbook descriptions. Therefore, we started to consider more direct and synchronized methods of molecular analysis with time sequence observations of cell behavior. In this report, we show how dynamic the cell response is when the cell is observed using a video microscope and how the resultant video analysis can be applied to molecular analysis. We also demonstrate a direct approach of analyzing molecular mechanisms underlying cell behavior, using our experiences as examples.

Rather than observing cells directly, one can employ optical microscopes [1] and, currently, a 2D video device can be used to detect the behavior of cells objectively. This can be recorded by video media as digital data of images at limited magnification [1,2]. Optical microscopic observation has a limit of resolution at approximately 200 nm [2,3] and can improve the apparent clarity of the images by video-enhanced contrast (VEC) image processing [2]. Recently, this resolution was improved by using far-field optical systems at 60 nm [4]. The digitized image data can be image processed by a computer in order to extract the essential aspects of the living mechanisms. These results triggered our desire to elucidate the underlying molecular mechanisms. However, current biochemical analyses must homogenize cells whose responses are different and not synchronized. In order to analyze each individual cell, very sensitive molecular analysis needs to be developed. Molecular dynamics or kinetics, even in minute regions, such as micro-organs, must also be clarified. Nanomedicine should be established with these clear conceptual but real dynamic images of biomedical phenomena from the nano- to macroscale. In this report, We review the research examples according to a flow-chart of new combinations of analytical approaches (Figure 1).

Keywords: image analysis, imaging, mass spectrometry, single cell dynamism, single molecular imaging, video-mass-scope, video microscope

Microvisualization of cell dynamism by video microscopes as a morphological approach

Science starts with the direct observation of objects. Video detection, unlike direct observation, which is 3D, is only an artificial 2D detector. However, video detection has advantages: it can be more sensitive at wider wavelengths; the

Figure 1. A new strategy for more straightforward analytical methodology for future medicine.

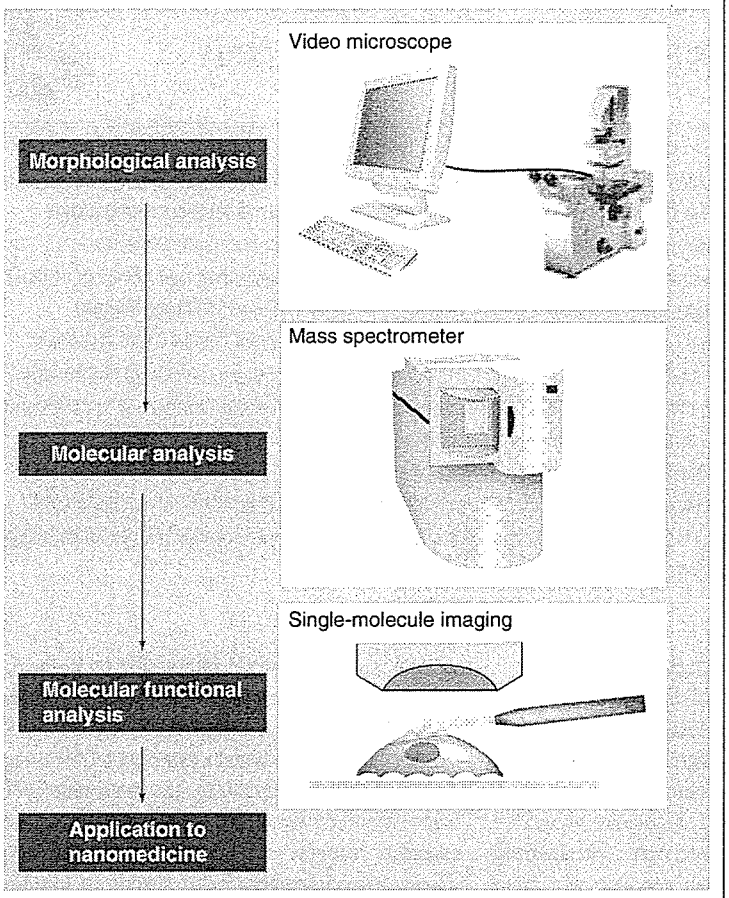

intensities at each point (pixel) of the detector (e.g., charge-coupled device) can be digitized to produce quantitative data; the huge amount of digitized data can be manipulated by computers for image analyses or image processing for our aims; and these data can be recorded precisely on data medias, such as video tape or DVD, with accurate time sequences. This methodology is now called 'bioimaging' [5,6].

One example of microvisualization of cell dynamism by video microscopes is shown in Figure 2. Neutrophils trap and digest invading microorganisms, a process called phagocytosis. Under the video microscope, the whole sequence of phagocytosis can be observed clearly over time [7]. We used an inverse-type fluorescence microscope (Axiovert 135-TV; Carl Zeiss, Germany) with a differential interference contrast (DIC) illumination system and the images were processed by VEC to produce clear images at limited magnification. Neutrophils moved slowly on the bottom of the culture dishes in various directions. When we observed this behavior for 1 day using a time-lapse video recorder, the cells spread and retracted pseudopodia to contact the surrounding substances, as if checking whether they are invading outsiders or safe insiders. We know that neutrophils guard our body from invaders; however, various dynamic aspects of the guarding behavior were impressive when we saw the video with a shortened time axis. When a neutrophil approached an invader, such as a zymosan (a boiled and processed yeast cell) [8], it formed a contact after migration (Figure 2A). After a lag time following the capture of a zymosan, the neutrophils extended pseudopodia around the zymosan (Figure 2B) and engulfed it into an intracellular space, called a phagosome (Figure 2C). The average time (n = 30) from pseudopodia attachment was approximately 34 s and the complete closure of phagosomes (n = 30) takes approximately 36 s. During the phagosome formation, rapid transport of microgranules to the phagosomes was observed and some granules in the peripheral area of the phagosome finally burst (Figure 2D) [7]. The photon-counting supersensitive video imaging for luminol-dependent chemiluminescence showed that the oxygen radicals were only released inside the phagosome [7]. Harmful molecules,

Figure 2. Sequence of phagocytosis (A & B) and exocytosis (C & D) of a neutrophil.

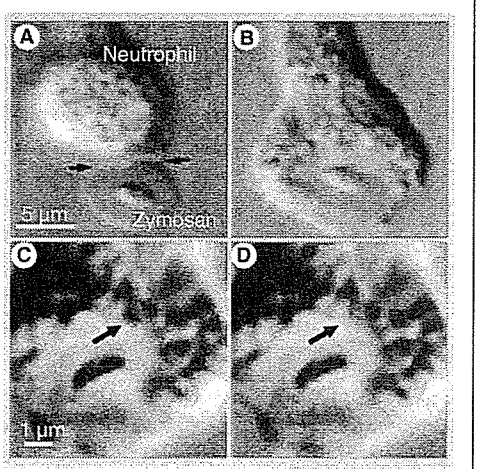

Arrowheads in **(A)** indicate extending pseudopodia. Arrows in **(C)** and **(D)** show the points where the popping of a microgranule (so called exocytosis) occurred.

such as superoxide species, are localized spatially inside of the phagosome only to protect neighboring cell bodies from attack. These tactics are very effective for neutrophils to attack invading micro-organisms. Since these programmed behaviors can be presumed to be the normal time course of the process, the period and shape of some medicinal treatments by molecules, such as drug candidates, various other factors and inhibitors, will show that changes in cellular behavior and shape will reflect the function of the factor.

However, video image analysis can be tedious and is not adequate for routine analyses, such as screening methods for new medicinal molecules. In Figure 3, we show the automating trial of imaging analysis for the potential application to mass screening for new medicinal molecules [9]. Eosinophils are another type of leukocyte that also perform phagocytosis. The automated sequential subtraction imaging method is used to extract the difference between two adjacent images (Figure 3Ai & ii). Figure 3Aiii depicts the result of the subtracted image that shows only moved parts of a cell, and this image was finally contrasted by binarization as Figure 3Aiv. Figure 3B shows the sequential images at 30-s intervals when an eosinophil located foreign particles. The curves in Figure 3B

Figure 3. Image analysis of eosinophil phagocytosis.

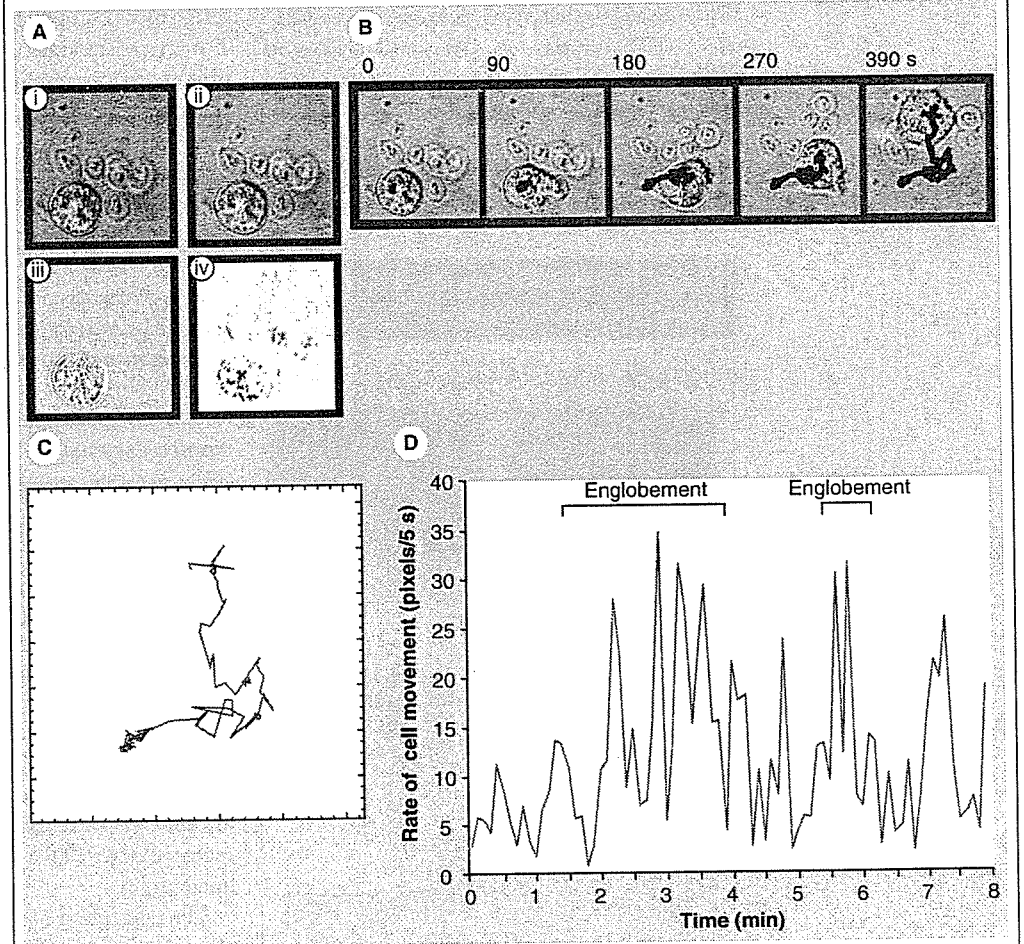

(A) Visualization of cell movement. (ii) was subtracted from the image of (i), and (iii) is the resultant image. The subtracted image (iv) was binarized in order to highlight the difference. **(B)** Sequential images of eosinophil phagocytosis. The images are placed sequentially from right to left. The bold lines in the images show the barycenter of the cell judged by the cell shape. **(C)** The trace of the barycenter. The trace was obtained from the sequential video images. **(D)** The rate of cell movement. The trace of the cell was measured at 5-s intervals and the rate of cell movement was calculated. The periods of englobement by the eosinophil are indicated, determined from the video images.

& 3C show the traces using the center of gravity of an eosinophil subtracted from the starting point. The drawn trace shows the cell's migration trajectory. Rate analysis of this trace in Figures 3B & 3C shows that cell movement is faster when it is attaching to a zymosan, as shown in Figure 3D.

This is an example of the automation of image analysis. Presently, various aimed automated morphological analyses using image processing can be performed using free software, such as the NIH image used here [101].

From morphological to molecular analysis: video & mass spectrometry combined analysis

Morphological aspect of the allergy response

Visualizing another type of exocytosis using a mast cell model, rat basophilic leukemia (RBL)-2H3 cells, a tumor analog of rat mucosal mast cells [10], has been studied (Figure 4) [11]. Here, we can again see the popping of microgranules at the moment of stimulation by an antibody or calcium ionophore, A23187 (Figure 4A). In order to apply these imaging results to molecular mechanisms, we counted the amount of popping during the time course. Two distinct peaks representing the number of microgranules that popped after A23187 stimulation, depending on its concentration (Figure 4B), were found. Thus, we concluded that there are two signaling pathways involved in the popping process triggered by calcium ion influx. Time-base counting of these exocytosis events in combination with the use of various inhibitors of cell signal transduction pathways revealed the sequential order of the molecular interplay in the signaling process. One process finishes fast (within 2 min), in which protein kinase C is involved, and another starts after the first process, with phospholipase D appearing to be involved [11,12]. This is an example of how we have used this time-based morphological analysis in molecular analysis, and further examples are cited in review articles [13].

Figure 4. Degranulation of mast cells by video microscopic imaging.

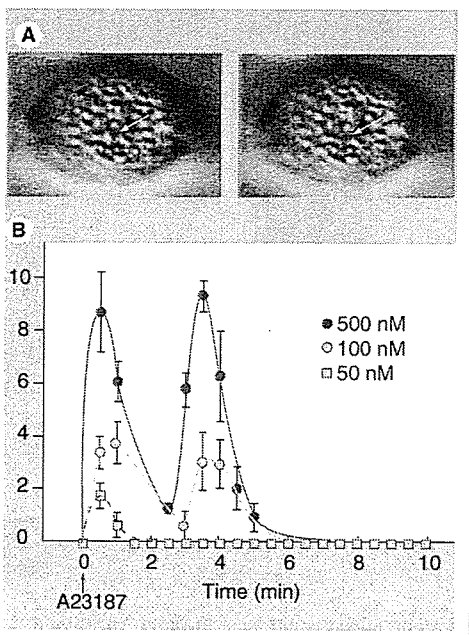

(A) RBL-2H3 cells were stimulated with A23187 and degranulation was observed by videomicroscopy. Arrows indicate the portion of degranulation. **(B)** Degranulation was digitized by counting the popped granules in the video images after different doses of A23187 stimulation.

As seen in our analysis, we need a known molecular mechanism or network in order to use the inhibitors that are known to block this process. Video analysis may show the roles of known molecules or the effect of some unknown molecules morphologically; however, it will not determine an unknown molecular mechanism.

From morphological observation to molecular analysis

Owing to the finding of two Nobel prize winners, Fenn and Tanaka, we are now in the age when molecules in solution, even if they have high molecular weight, can be detected by mass spectrometry [14,15]. Matrix-assisted laser desorption-ionization time of flight (MALDI-TOF) mass spectrometry (MS) is very sensitive and is suited to the direct detection of molecules (e.g., peptides and proteins, in cells or tissues). By scanning the laser beam for ionization, molecular mapping can be performed [16] and dynamic secondary ion mass spectrometry (SIMS) has also been applied to imaging [17].

The detection of secreting molecules in a single cell was examined using MALDI-TOF/MS, which is called single-cell MALDI-TOF/MS [18,19]. Many attempts using single-cell MALDI-TOF/MS have been published previously [20–22]. For large cells, such as neurons, single-cell handling is easy, but regular-sized cells (~10 µm) are too small to trace their positions in the matrix crystallizing process.

Figure 5A shows an experimental process for microsucking of a single cell into a capillary pipette to transport the cell from a culture dish to the sample plate of a MALDI-TOF/MS. A droplet of the matrix solution (in this case, 2,5-dihydroxybenzoic acid [DHB]-saturated solution) was dropped onto the single cell on a sample plate. As shown in Figure 5B, matrix DHB started to crystallize owing to vaporization of a tiny amount of solvent and the cell was surrounded by these microcrystals of water-soluble matrix (Figure 5Bi–iii). By tracing the position of the cell under a microscope, this sample plate was introduced into the vacuum sample chamber of the MALDI-TOF/MS, to be ionized by spot irradiation from a nitrogen-pulse laser.

Figure 5. Single cell MALDI-TOF/MS analysis.

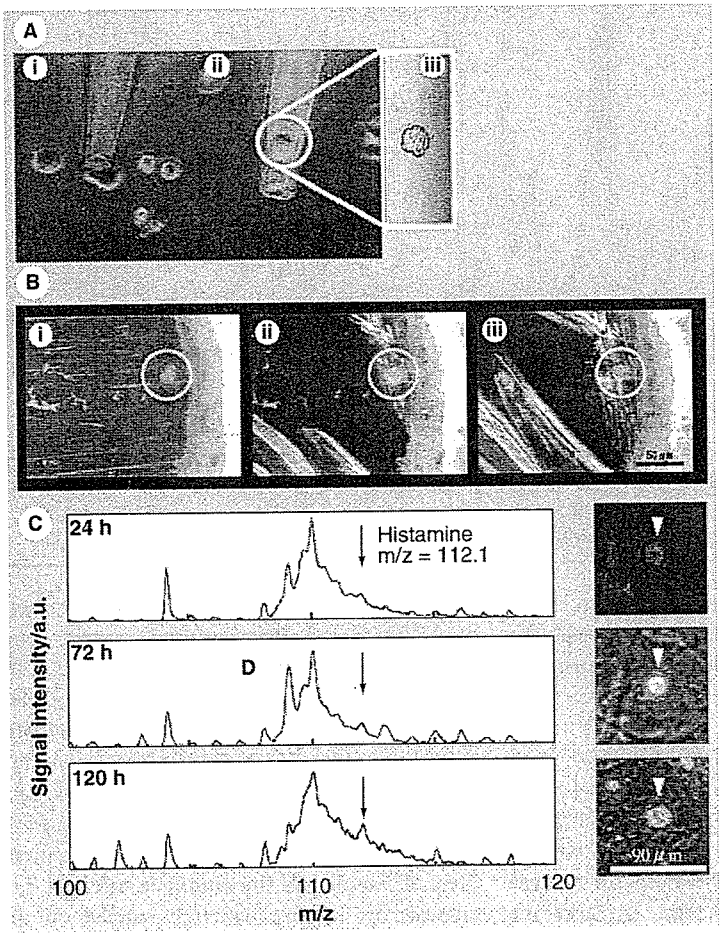

(A) A mast cell was collected by microsuction. **(B)** An isolated cell (indicated by the circles) was extracted by matrix solution (i–iii; crystals of the matrix are growing). **(C)** Morphology of a mast cell (right pictures) and MS spectra. MALDI-TOF/MS was used in positive mode.
MALDI: Matrix-assisted laser desorption-ionization; MS: Mass spectrometry; TOF: Time of flight.

Many histone-related basic proteins and basic molecules were detected in positive mode [9]. The molecular species in a cell should be numerous; however, there were fewer mass peaks detected than expected. Several possibilities could have accounted for this: the presence of salt in the buffer solution for cells appears to prohibit the ionization of various molecules; when the easily ionized molecule is dominant in a cell, the molecule(s) dominate the total ionization and mask the detection of other target molecules. In these detected molecules, we focused on the detection of histamine (m/z = 112.1) because, as the chemical mediator of allergy, it is concentrated selectively in the microgranules in the cell and the quantity reflects the cell maturation process. Figure 5C demonstrates that a bone marrow-derived mast cell showed an increased peak of histamine after accelerated maturation on the fibroblast layer during 1 week. Morphological observation by a video microscope also showed that the number of microgranules in the cell increased according to the incubation time (Figure 5C) (see photographs). Rubakhin and colleagues used vesicles from the exocrine atrial gland of *Aplysia californica* to detect a wide range of bioactive peptides within each vesicle [23].

A microchannel plate (MCP), which is not sensitive for higher mass molecules, is usually used as the detector of MALDI-TOF/MS. In place of MCP, a new cryogenic detection has been developed that has mass-independent sensitivity [24]. Using this new detector, MS imaging for proteins in a mouse brain was performed (Figure 6). Three dominant proteins at 12.2, 14.1 and 15.0 kDa were mapped to show that the 14.1-kDa molecules originated predominantly from the white matter of the brain and the 15.0-kDa molecules originated from the gray matter, while the 12.2-kDa proteins were distributed more evenly [24].

The MALDI-TOF/MS method has a distinct advantage in analyzing the whole molecular weight of components with less fragmentation at higher sensitivity, but a molecular collision tool and a method to identify the molecule is not so common, unless a new MALDI-TOF/TOF is used. The concept of single-cell MALDI-TOF/MS analysis combined with videovisualization appeared to provide a basis for a probable future method; however, we should be careful because the ionization process of target molecules in a cell body may include easily ionizing molecules

Figure 6. MALDI images of three proteins in mouse brain tissue.

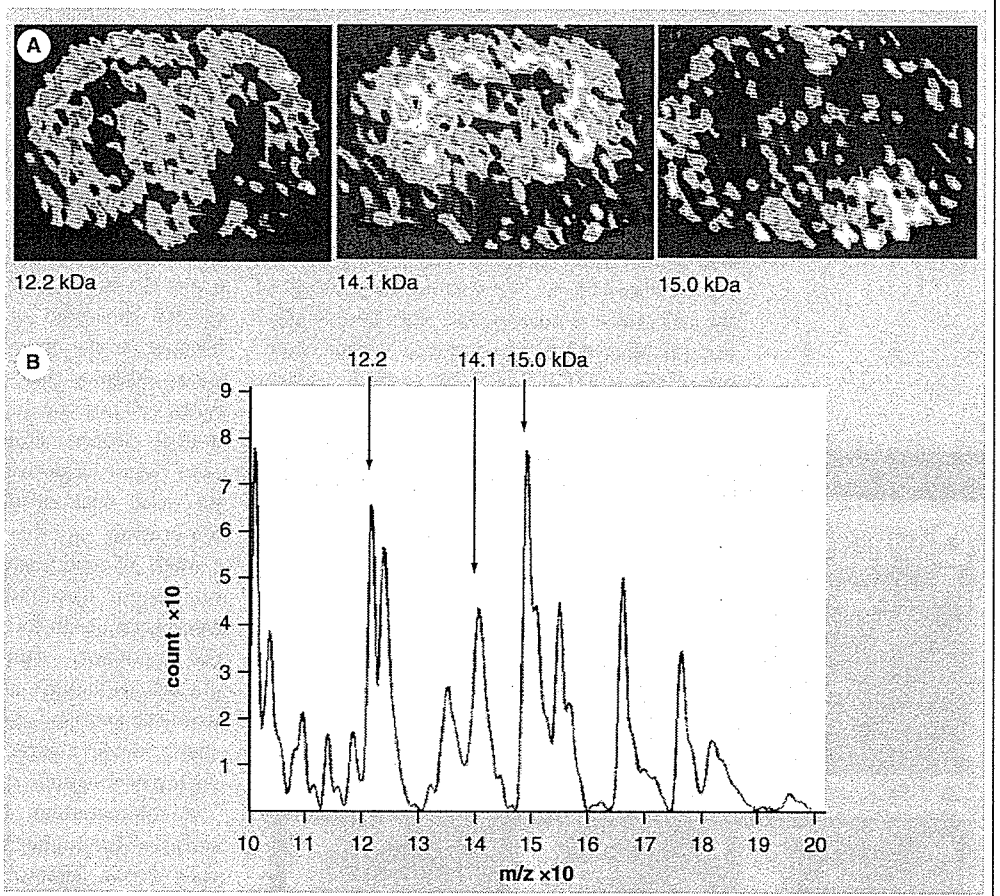

(A) A 12-µm thick section of frozen mouse brain attached onto a MALDI plate was covered with an array of sinapinic acid matrix droplets. The plate was moved in the x- and y-axis and the laser was focused to the center of each spot. The mass spectrum, as shown in **(B)**, was obtained at each spot. The peak intensity corresponding to 12.2-, 14.1- and 15.0-kDa proteins was obtained from each spectrum and was plotted onto the brain image: white represents high intensity, gray represents medium intensity and black represents low intensity. MALDI: Matrix-assisted laser desorption-ionization.

that could monopolize the ionization, while lipid molecules of cell membranes and salts in the cytosol may prohibit the ionization of target molecules.

Simultaneous analysis of molecules & morphology: video-mass-scope

In order to obtain steady ionization of target molecules and analytical versatility, we are now developing a more direct way to analyze cellular contents using MS. Figure 5A shows one experimental setting for our concept of 'video-mass-scope' [9], by which simultaneous video microscopic observation and mass spectrometric analyses are conducted [25]. Since the level of molecules secreted from cells is very low, we need to innovate a preconcentration (with desalting) and deproteinization procedure. Many trials have resulted in preconcentrating tips for biological fluids [26–30]. We developed gold-coated grass capillary nanoelectrospray tips, which were packed originally with high porosity reversed-phase resin and mixed mode (cation exchange and reversed-phase) resin (Figure 7A) [25]. These tips make it possible to desalt and concentrate a few microliters of sample and the sample is enforced into analysis by elution, which is carried out by nanospraying. By observing the cell dynamism by video microscopes, secreted molecules from cells in 1 µl of culture buffer were sucked into the tips and analyzed simultaneously by a mass spectrometer at a sensitivity of 0.25 pg/µl. Figure 7B shows the total results when we

Figure 7. Video-mass-scope analysis of secreted molecules.

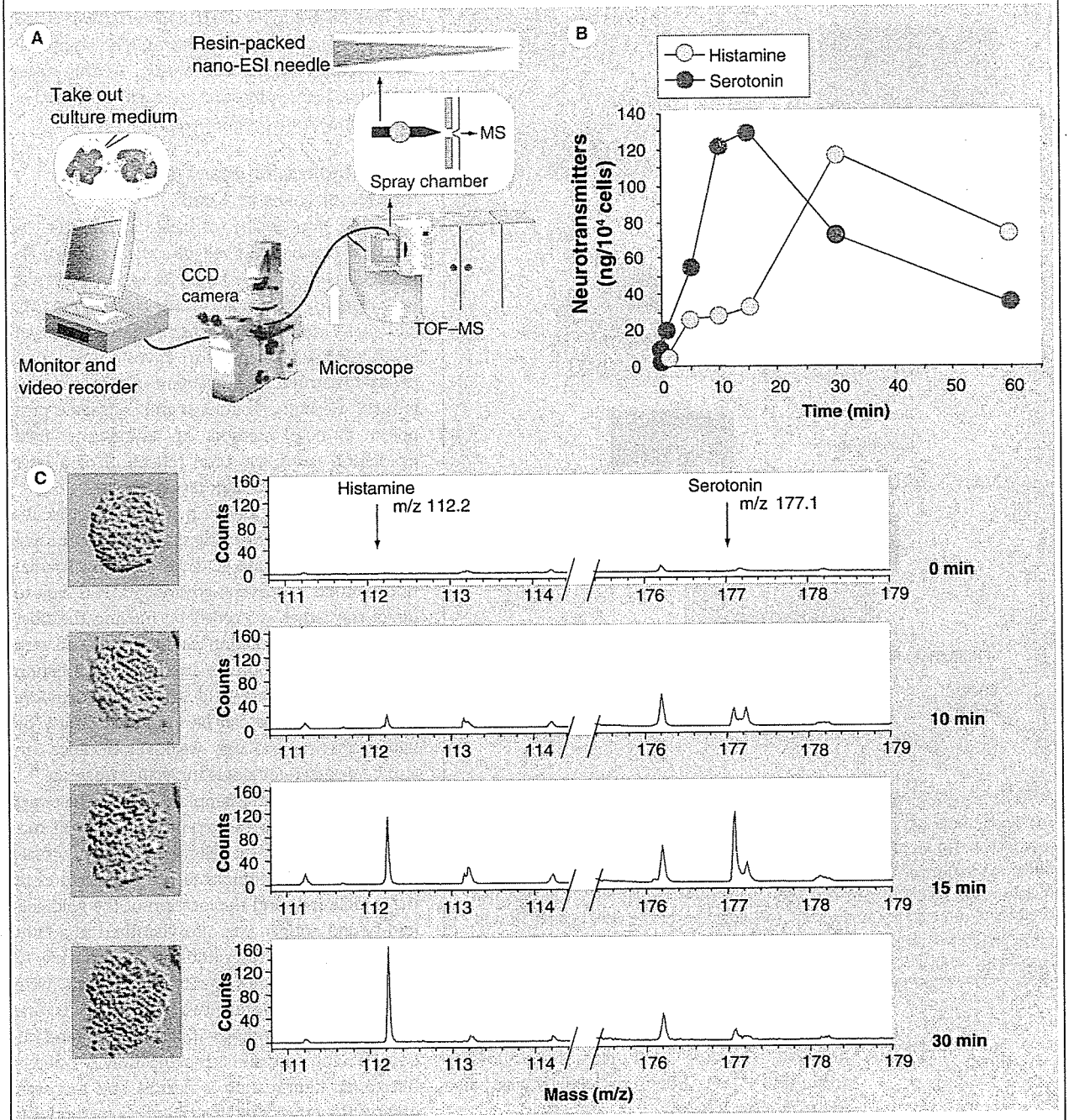

(A) Scheme of video-mass scope and the resin-packed eloctrospray tip. **(B)** Video images of A23187-stimulated RBL-2H3 cells and MS spectra. The culture medium of the cells under videomicroscopic observation was isolated sequentially, desalted and concentrated using the electrospraty tips, then analyzed by MS. The arrows indicate histamine and serotonin secreted from the cells. **(C)** Histamine and serotonin accumulation after stimulation. The amount of the molecules was calculated from the peak areas of the MS spectra.
CCD: Charge-coupled device; ESI: Electrospray ionization; MS: Mass spectrometry; TOF: Time of flight.

applied this video-mass-scope to the analysis of the allergy response of a mast cell model, using rat basophilic leukemia RBL-2H3 cells [25]. After stimulation with a calcium ionophore, A23187, the cell began exocytosis, as seen in the video images of the left row of Figure 7C [25]. By simultaneous mass spectrometric detection of molecules in the cell

Figure 8. System of single molecular imaging.

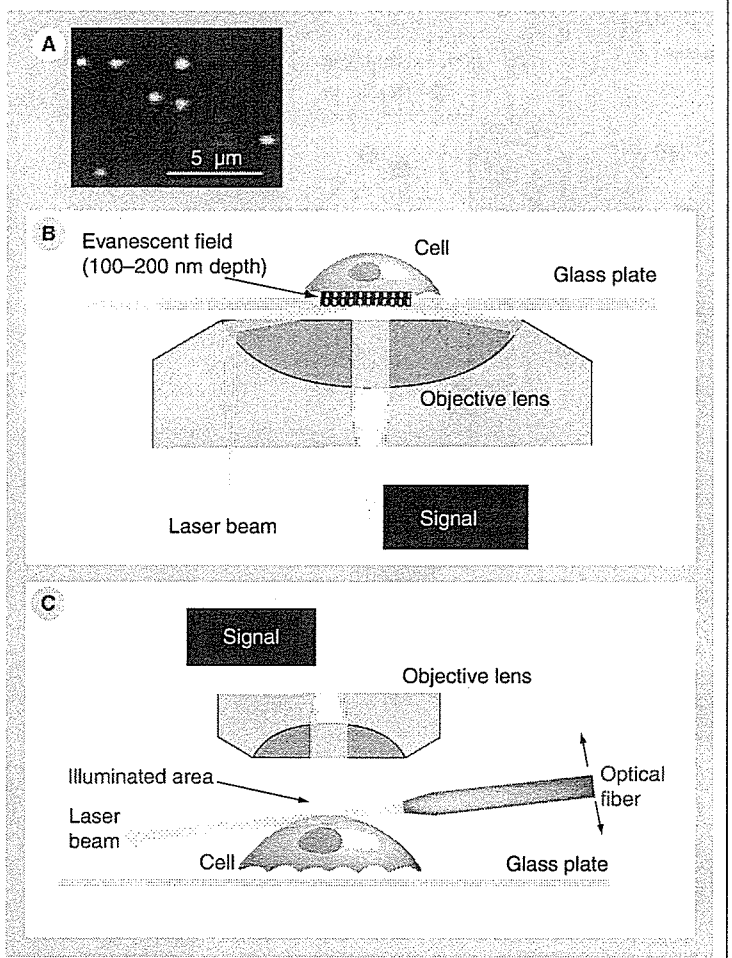

(A) Single-molecule observation of Cy3-labeled ATP molecules attached to myosin [31]. **(B)** and **(C)** show the schemes of objective-type total internal reflection fluorescence microscopy [35] and optical fiber illumination fluorescence microscopy, respectively. Objective lenses are shown as gray half circles and outlined arrows indicate the directions of the laser beams. Dotted areas are an evanescent field induced by total internal reflection in **(B)** and a laser beam-irradiated by fiber optics in **(C)**.

medium, histamine and serotonin were detected, showing their secretion following stimulation [25]. These molecules were also identified by MS/MS.

In accordance with these images of exocytosis, the time course of mass peaks of histamine and serotonin showed increasing trends at 30 and 10 min, respectively (Figure 7B). The accumulation curves also indicate that the mechanisms of histamine and serotonin release were different, as histamine showed a stepwise increase in accordance with the two-peak popping time course (as seen in the video observation in Figure 4B) [11], in contrast to serotonin [25]. These results suggest that the pathways and mechanisms of secretion and release of histamine are different. Therefore, we now have a more direct and versatile method to analyze molecular mechanisms, with a simultaneous morphological observation. At this stage, video-mass-scope remains as such and further developments are progressing.

Single molecular imaging observing molecular tasks in a cell

When we have finally identified a molecule, its function can be observed directly by the single molecular imaging method. Pioneering work was performed by Yanagida's group (Figure 8A) [31,32], and many molecular mechanisms were imaged beautifully, such as the actin–myosin interaction [33] and the rotating movement of a motor protein [34]. Recently, Tokunaga and colleagues proposed a new method of evanescent field irradiation using the total reflection of a laser beam in an objective lens (Figure 8B) [35].

We proposed a different method of laser irradiation for this imaging using single fiber optics as a microspot light (Figure 8C & 9A) [36]. This irradiation method has several advantages: it is easy to direct the target as needed by moving the fiber optics; and the irradiation can be introduced with almost no background scattering of irradiation light, similar to dark-field irradiation, therefore very fine structures can be visualized clearly by light scattering and very weak fluorescence can also be detected for single molecular imaging.

Figure 9B shows an example of tracing the target molecule bound to the receptor on the cell surface. The surface of the cell membrane was visualized by light reflection, as seen in the pictures in the middle row, and the location of the gold colloid-bound antigen was also visualized as a faint dot in the same pictures (indicated by an arrow to the circle). The movements of the dots were traced (Figure 9B) to show two species of dots: one is fluctuating by binding with the receptor and the other is not bound and is moving away [36]. Single fiber-optic illumination is flexible and can even observe the upper side of a cell. This method was also applied to analyzing molecular behavior in living cells by introducing a fusion gene that encodes green fluorescent protein (GFP)-tagged signal transducer and activator of transcription (STAT)1 [37]. STAT1 localizes at the cytosol when the cell receives no stimuli. Once the cells have been stimulated with interferon (IFN)-α, STAT1 molecules are recruited to the IFN-α receptor and phosphorylated by associated kinases. They then form a dimer and leave the receptor (these processes

Figure 9. Single-molecule imaging by single fiber-optic illumination.

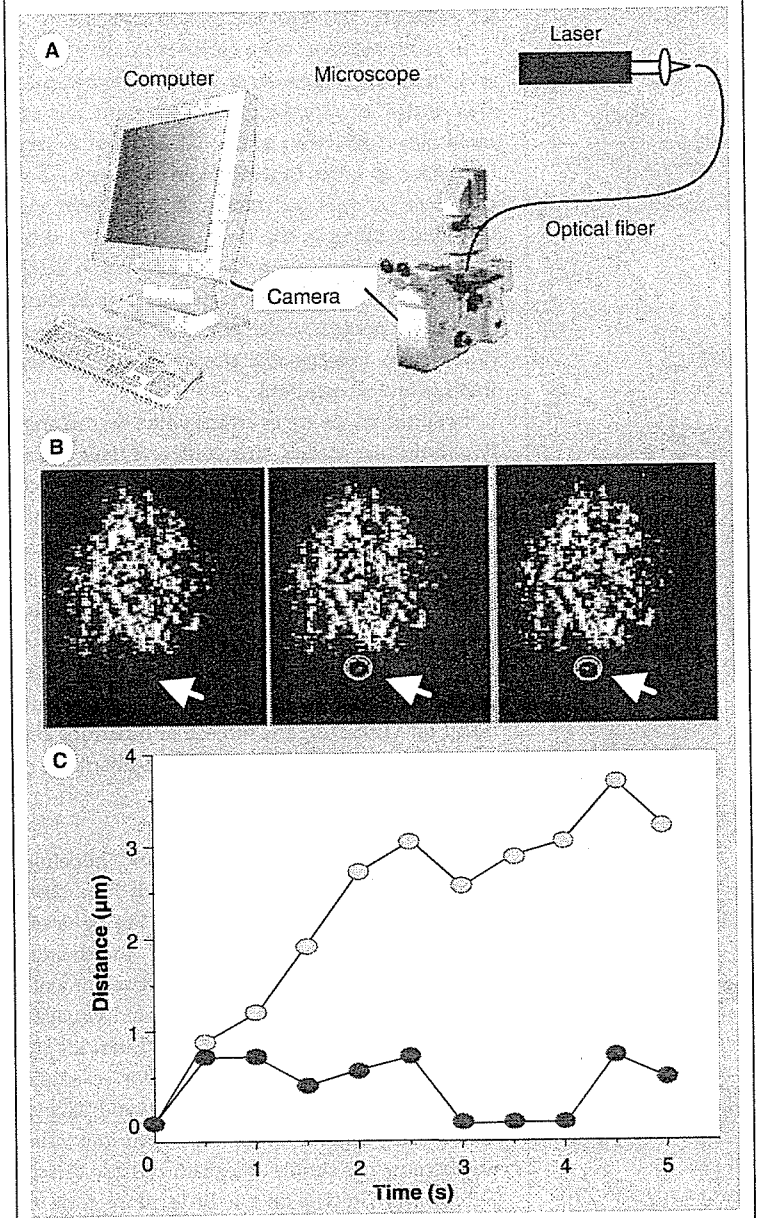

(A) Scheme of single fiber optics illumination-mediated single molecule imaging system. **(B)** Video image of gold colloid labeled receptor molecule. The spot inside the circle is the target. **(C)** Traces of gold colloids. The light purple circles show free colloids that left from the cell, and the dark purple circles represent receptor-bound colloids that stay on the cells.

are indicated schematically in Figure 10A) [37]. We observed many light spots with short lives that correspond to a single GFP–STAT1 molecule (Figure 10B). Among these spots, the brightness of some increased twice and decreased, indicating that the molecule dimerized on a receptor site and then moved away (Figure 10C) [37].

Application of visualization analysis: nanokinetics for nanomedicine

Now we have a clear image of the molecular mechanism of cell dynamism and the related molecular species by the aforementioned methodologies. The application step can now proceed, which will provide some of the information required for nanomedicine design, including the molecular dynamics within a tiny area, such as a single cell space, which is called 'nanokinetics'.

The target molecule must perform its task in a dynamic way in a cell or within micro-organs in a cell. Nanokinetics has various meanings, such as molecular changes in a nanoscale space, molecular transport in nanospace or morphological changes in nanospace.

Videovisualization, which records the time axis, is a useful method for not only observing but also analyzing nanokinetics. One problem is how to visualize the molecule in the target. Adducting fluorescent probes to the target molecule sometimes perturbs real dynamism of the molecule owing to the attachment of a large-sized probe or structural modification.

When the medicinal molecule on the target has its own fluorescence, the situation is easy. Quinacrine, whose derivative was used formerly as an antimalarial drug, is weakly basic and incorporated selectively into acidic microgranules in RBL-2H3 cells [11]. At different outside concentrations of quinacrine, its transport into a cell was traced by video detection (Figure 11A) [38]. The increasing concentration of quinacrine inside a cell was different depending on the region of cytosol or granules and depending on the initial concentration of the medium. We can see that quinacrine incorporates selectively into granules more easily than it remains in the cytosol [38].

By applying the hypothesis of a two-compartment model of transportation of molecules (Figure 11B), it was found that the first step, transport through the cell membrane, is an energy-requiring transporting process, such as active transport; however, the second step of transport through the microgranule membrane is pH gradient-dependent passive transport [38]. These fundamental analyses of kinetics will establish quantitative dynamic understanding and could also predict the time course of molecular transport through the analyzed parameters of the process, which is very important for establishing nanomedicinal treatment.